



Numerical Modeling of Multiphysics Field in Conventional and Stationary Shoulder Friction Stir Welding of Al-Cu Alloy

Jiaqing You, Yunqiang Zhao, Chunlin Dong, Yaoyong Yi, and Yunhai Su

Submitted: 13 December 2020 / Revised: 1 February 2021 / Accepted: 1 March 2021 / Published online: 24 March 2021

In robotic friction stir welding, high rotational speed is constantly employed to reduce both robot torque and the welding load. In this paper, a three-dimensional coupled thermo-mechanical model is developed. This model analyzes the multiphysics field in both friction stir welding and stationary shoulder friction stir welding at relatively high rotational speeds. Both experimental and numerical results indicate that the stationary shoulder friction stir welding joint has homogenous microstructure and temperature gradient distribution. Further research finds the peak temperature in the nugget zone of stationary shoulder friction stir welding and friction stir welding is 490° and 530°, respectively. Meanwhile, the effective strain of the stationary shoulder friction stir welding joint is lower when compared to the friction stir welding. However, the strain rate is higher. While being reduced along the thickness direction, the strongest material flow velocity is observed in the top surface of the workpiece. Stationary shoulder friction stir welding is shown as a favorable process for obtaining the homogeneity of the microstructure and reducing joint softening.

Keywords friction stir welding, material flow, numerical simulation, stationary shoulder friction stir welding, strain rate, thermal cycle

1. Introduction

Friction stir welding (FSW) is an advanced welding technology developed by The Welding Institute in 1991. During FSW, friction heat is generated due to the frictional forces between the rotational tool and the workpiece. The material located in the proximity of the contact surfaces is eventually plasticized. The plasticized material is combined under the action of the stirring tool (Ref 1, 2). The peak temperature in the weld zone is lower than the material's melting point, while the defects such as liquefaction cracks and pores can be avoided. Thus, FSW is widely utilized for welding of aluminum alloys. On the other hand, stationary shoulder friction stir welding (SSFSW) is a novel welding technique based on the FSW method. The schematics of the FSW and SSFSW are presented in Fig. 1. The heat generation during the conventional FSW mainly originates from both contact

between the pin and the workpiece, and the shoulder and the workpiece (Fig. 1a) (Ref 3). Owing to the difference in the contact area and the relative velocity, more heat input is generated by the rotational shoulder than the pin, which can reach up to 70% of the total welding power (Ref 4). During the SSFSW, the shoulder remains stationary, while the tool slides on the weld surface (Fig. 1b). Thus, the shoulder contributes less to heat generation and enables the process to result in a more concentrated heat input in the proximity of the pin (Ref 5).

In recent years, many investigations of SSFSW application in aluminum alloys emerged. Li et al. (Ref 6) studied the change of 2219-T6 tensile strength with an increase in rotational speeds. The results demonstrated that tensile samples fractured in the softening zone of the joints. Sun et al. (Ref 7) reported residual stress distributions during the SSFSW and FSW. The results indicated that the SSFSW joints had a narrower tensile region and a sharper residual stress profile due to the relatively small thermal field. Wu et al. (Ref 8) compared the microstructure and the mechanical properties of SSFSW and FSW joints. Their results revealed narrower heat-affected zone (HAZ) and thermo-mechanically affected zone (TMAZ) obtained in the SSFSW joints, while welds demonstrated increased tensile strength and microhardness values. However, the temperature distribution and the welding thermal cycle were not revealed in the process. Sinhmar and Dwivedi (Ref 9) studied the mechanical behavior of SSFSW and the FSW. The author observed that the nugget zone (NZ)/TMAZ interface is additionally mixed in the SSFSW joint. Meanwhile, tensile test results demonstrated that the fracture location was present at the HAZ and NZ/TMAZ interface for FSW and SSFSW techniques, respectively. Therefore, it can be concluded that both welding thermal cycles and the material flow have a significant influence on the structure and mechanical properties of materials. Numerical simulation has proven as an effective method for investigating the FSW process. Su et al. (Ref 10) analyzed thermal and material flow of different pin profiles.

Jiaqing You, Yunqiang Zhao, and Chunlin Dong, Department of Materials Science and Engineering, Shenyang University of Technology, Shenyang 110870 Liaoning, China; and Guangdong Provincial Key Laboratory of Advanced Welding Technology, China-Ukraine institute of Welding, Guangdong Academy of Sciences, Guangzhou 510651, China; and **Yaoyong Yi**, Guangdong Provincial Key Laboratory of Advanced Welding Technology, China-Ukraine institute of Welding, Guangdong Academy of Sciences, Guangzhou 510651, China; and **Yunhai Su**, Department of Materials Science and Engineering, Shenyang University of Technology, Shenyang 110870 Liaoning, China. Contact e-mails: zhaoyq@gwi.gd.cn and dongchl@gwi.gd.cn.

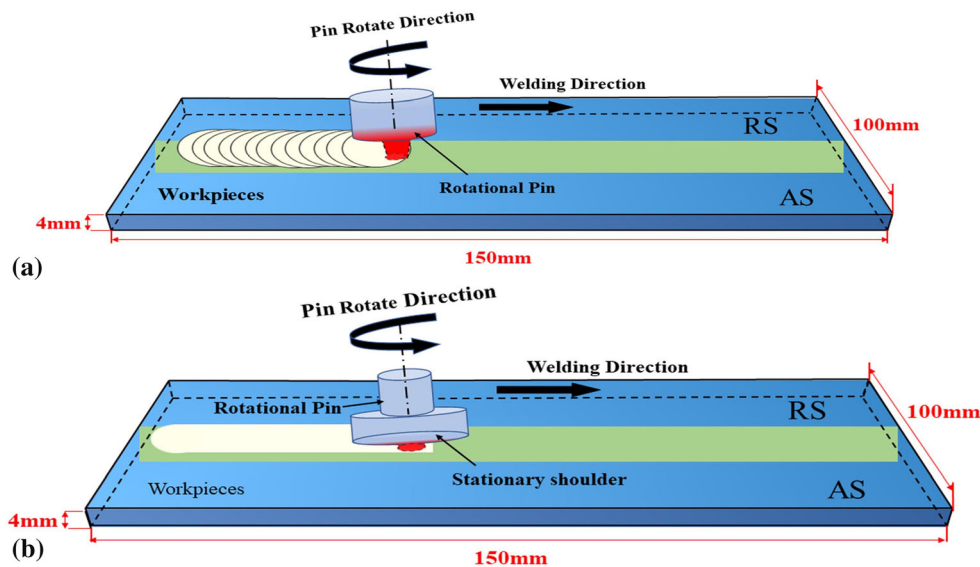


Fig. 1. Schematic welding process representation: (a) FSW (b) SSFSW

The authors found that the stir action of a conical tool demonstrated enhanced material flow when compared to the triflate tool. Fratini et al. (Ref 11) investigated the material flow through numerical simulations and experiments. The study illustrated actual material bonding in the advancing side (AS) of the FSW joints, while conical pins determine a more effective material flow. B. Vicharapu et al. (Ref 12) investigated residual stress distribution in SSFSW and FSW processes. The authors observed approximately 10 to 20% reduction of peak residual stresses in SSFSW. Li et al. (Ref 13) numerically investigated material movement and equivalent plastic strain during stationary shoulder friction stir lap welding. According to the conducted literature survey on SSFSW, mainly residual strength and plastic strain are investigated in detail. However, material flow behavior, strain rate, and microstructure formation still need to be adequately explored, especially at high rotational speeds.

With the development of intelligent manufacturing, high rotational speed FSW combined with industrial robots is considered as a promising technology. This is mostly due to lower welding torque requirements that are accompanied by relatively high rotational speeds. Therefore, it is necessary to investigate the multiphysics field during high rotational speed SSFSW and FSW processes. To adequately investigate the thermal cycle, material flow behavior, and the effective strain characteristics of FSW and SSFSW at relatively high rotational speeds, a three-dimensional thermo-mechanical coupled model is developed. The proposed model is validated against the experimental data of thermal cycles at predefined points.

2. Experimental Procedure

The base material (BM) used in this study is 2219-T6 aluminum alloy. The nominal compositions are shown in Table 1.

The dimension of the workpieces was 150 mm × 100 mm × 4 mm, as shown in Fig. 1. The schematics of the FSW

Table 1 Nominal composition of 2219-T6

Cu	Mn	Si	Zr	Fe	Zn	V	Ti	Al
6.48	0.32	0.49	0.2	0.23	0.04	0.08	0.06	Bal.

and SSFSW tools are provided in Fig. 2. Both tools had a 12.0-mm shoulder and a 3.9-mm-long conical pin, while the top and the bottom pin diameters were 5.0 mm and 3.0 mm, respectively. The thermal cycle was measured by using K-type thermocouples embed in holes, which have a 3.0 mm depth measured from the top surface of the workpiece and were located 7.5 mm (A) and 9.0 mm (B) from the weld line (Fig. 2). Based on the previous investigations, a 2000-RPM rotational and 100 mm/min welding speeds were selected as experimental parameters. After welding, the metallographic samples were polished and etched with Keller's reagent (2.5% HNO₃, 1% HF, 1.5% HCl, 90% H₂O, volume fraction). The microstructure was observed through optical microscope (OM, Axio Imager M2m), while hardness was tested by Vickers hardness tester (Buehler VH1202) with a 300g load for the duration of 10s.

3. Numerical Model

The main differences between the FSW and SSFSW are presented in Fig. 1. According to their own characteristics, the numerical model based on the finite element analysis software DEDORM-3DTM was established to illustrate both processes. In this paper, an arbitrary Lagrangian Eulerian (ALE) was chosen for the simulation, while ensuring that the simulation parameters were consistent with the parameters from the welding experiment (Ref 14).

Figure 3 depicts the geometric model utilized for the numerical simulation. It was composed of two parts: the workpiece and the welding tool. The material model of the

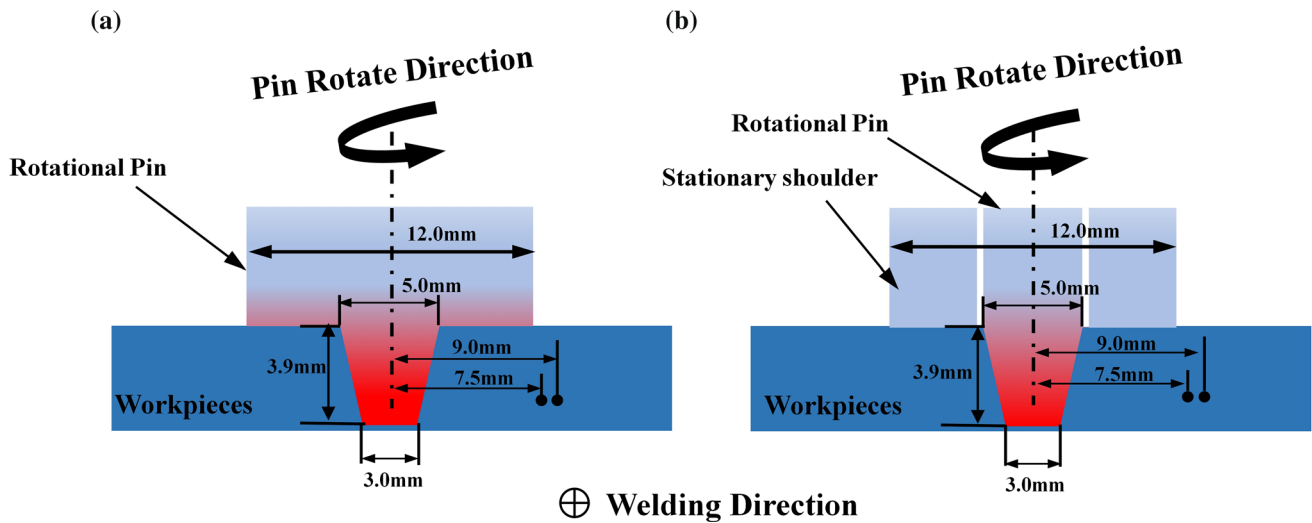


Fig. 2. Schematic representation of tool and thermocouple points: (a) FSW (b) SSFSW

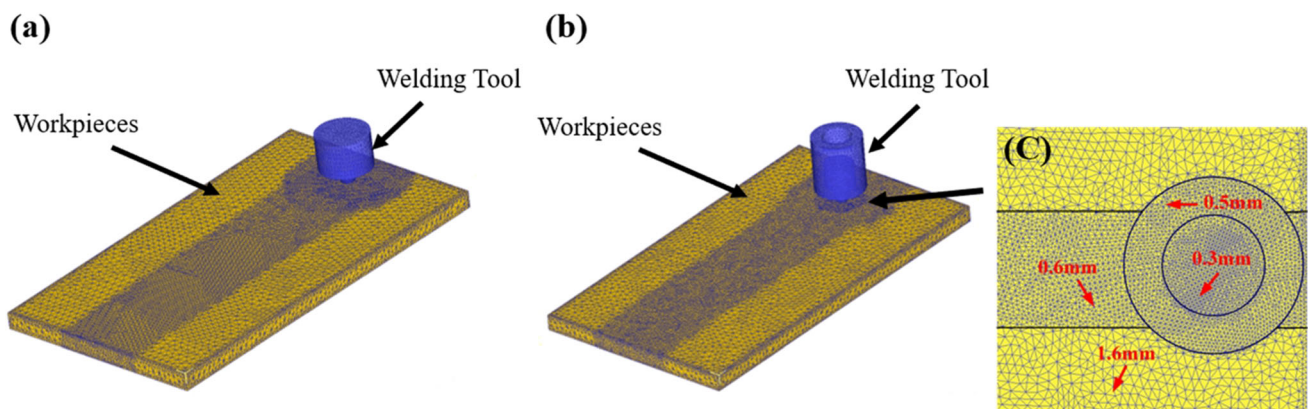


Fig. 3. Geometric simulation model: (a) FSW; (b) SSFSW; (c) the detail in the concentrated mesh

workpiece was defined as visco-plastic. On the other hand, the welding tool was defined as purely rigid material. Moreover, the workpiece was divided into 140 000 tetrahedral mesh-elements with size varying from 0.3 to 1.6 mm, while the welding tool was meshed with 40 000 tetrahedral mesh-elements, with mesh size varying from 0.2 to 0.6 mm. In order to improve the calculation accuracy, the welding center was locally refined, while adaptive re-meshing was simultaneously employed (see Fig. 3c).

Owing to simultaneous rotational and traversal movement of the welding tool during the FSW process, the mechanism of friction is relatively complicated. According to the previous studies (Ref 14, 15), the friction force in a constant shear model was applied:

$$f = mk \quad (\text{Eq 1})$$

where f is the frictional stress, m is the friction factor, and k is the shear yield stress. The most suitable shear friction factor of 0.46 was chosen based on the previous study (Ref 16). The stationary shoulder generated negligible heat. Thus, the coefficient of friction for the shoulder was taken as 0 in this simulation.

The Arrhenius constitutive material model used to illustrate the effect of temperature and strain rate on the flow stress was

applied for this numerical simulation. The Arrhenius constitutive material model can be written as:

$$\bar{\epsilon} = A[\sinh(\alpha\sigma)]^n \exp\left(-\frac{Q}{RT}\right) \quad (\text{Eq 2})$$

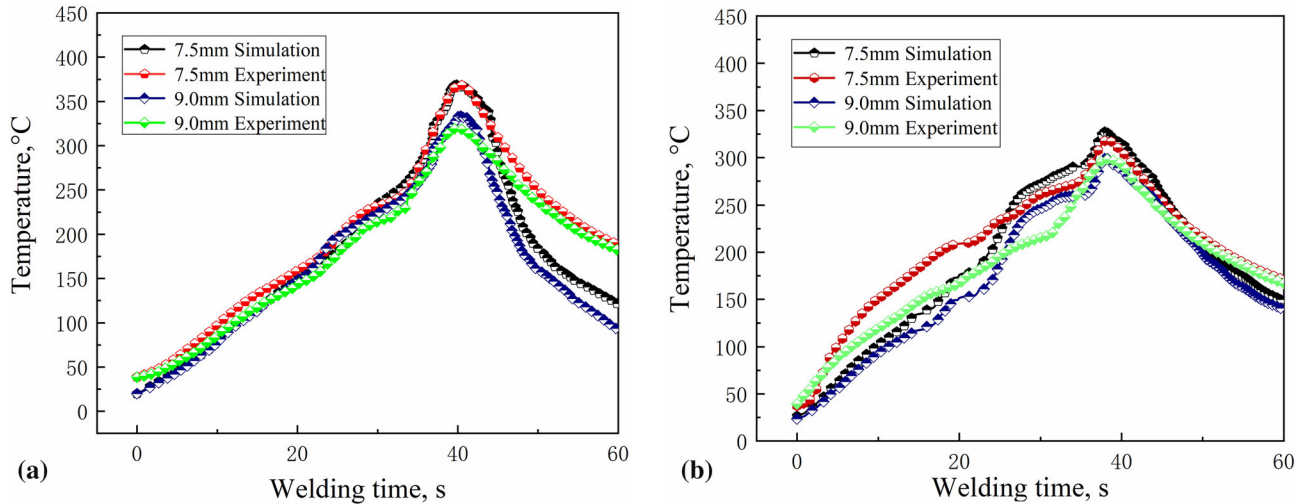
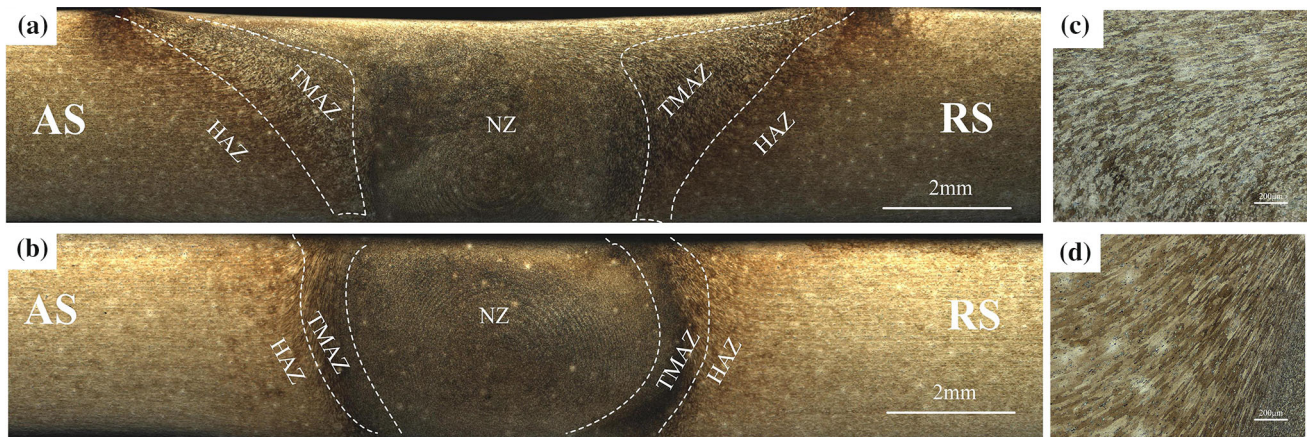
where $\bar{\epsilon}$ (s^{-1}) is the plastic strain rate, $A = 1.369 \times 10^{11}$ is the structure factor, $\alpha = 0.0147$ is the stress level parameter, $n = 6.65$ is the stress exponent, $Q = 159737$ J/mol is the activation energy, $R = 8.314$ J/mol K is the gas constant, and $T(K)$ is the temperature (Ref 17).

In addition, the initial temperature of the workpiece and the welding tool was 30 °C. A constant interface heat exchange coefficient of 11 N/mm °C was utilized for the contact surface between the workpiece and the welding tool. The heat exchange coefficient between the workpiece and the surrounding environment was 0.02 N/mm °C. It should be mentioned that the heat convection coefficient between the bottom part of the workpiece and the surrounding environment was taken as 1 N/mm °C (Ref 18). The thermal properties of the workpiece (solid state) are listed in Table 2 (Ref 19).

In order to validate the feasibility of the numerical model, experimental data for predefined locations are compared against the numerical results, and the temperature curves are shown in Fig. 4. Good correlation between the measured temperature

Table 2 Thermal properties of 2219 aluminum at different temperatures

Temperature, °C	20	100	200	300	400	≥ 500
Young's modulus, GPa	73	71	68	63	57	52
Poisson's ratio	0.33	0.33	0.34	0.34	0.35	0.35
Density, Kg/m ³	2870	2850	2800	2760	2730	2710
Specific heat, J/Kg °C	860	900	945	982	1026	1260
Thermal conductivity, W/m °C	144.0	152.9	161.0	166.1	169.0	170.0

**Fig. 4.** Comparisons between measured temperature results and the calculated results from the simulation at various positions**Fig. 5.** Microstructure cross section characterization: (a) FSW, (b) SSFSW, (c) TMAZ (AS in FSW), and (d) TMAZ (AS in SSFSW)

data and the numerical results is observed. Therefore, it is demonstrated that the welding process of the FSW and the SSFSW can be adequately described via developed numerical model.

4. Results

Figure 5 shows the microstructure of the cross section of FSW and SSFSW joints at 2000 rpm with a constant welding speed of 100 mm/min. Both the FSW and SSFSW joints are divided into several parts by the dash line: heat-affected zone

(HAZ), thermal-mechanically affected zone (TMAZ), and the nugget zone (NZ). The shape of the FSW and SSFSW joints areas is consistent with the tool profile. According to Fig. 5(c) and (d), TMAZ grains are elongated in a certain direction, while the characterization of TMAZ in the SSFSW is sharper. In addition, a decrease in the TMAZ and HAZ regions during the SSFSW is observed.

The cross-sectional hardness contour maps of the FSW and SSFSW joints are shown in Fig. 6. Although grains in the NZ are refined, the softening is still noticeable, which is mainly due to the second phase particles dissolved during the welding thermal cycle. The minimum hardness of these joints can be

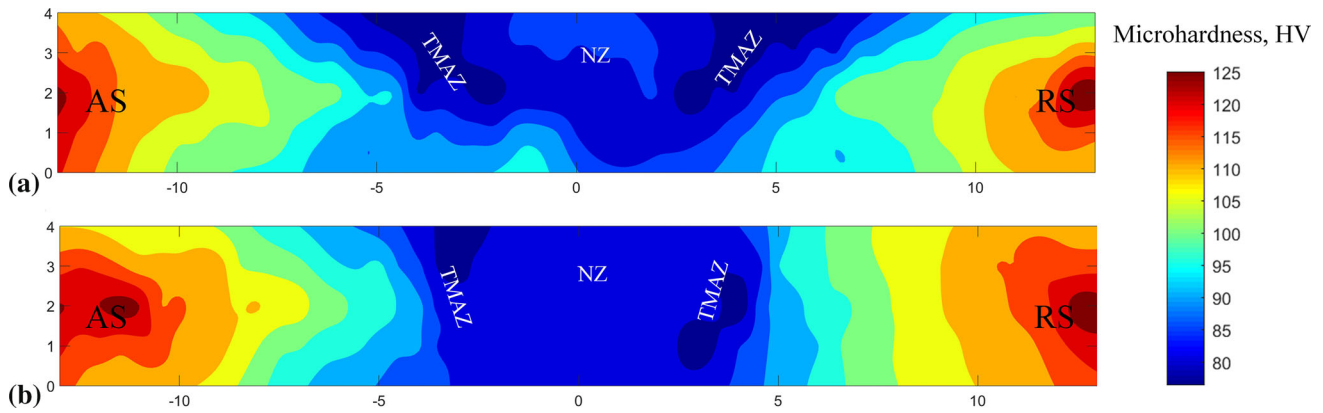


Fig. 6. Cross-sectional hardness contour maps from welds produced with: (a) FSW and (b) SSFSW

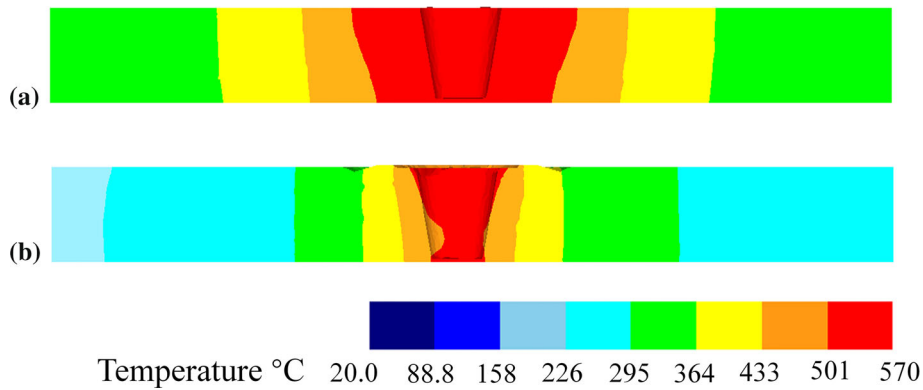


Fig. 7. Dwelling time temperature distributions in the workpiece: (a) FSW, (b) SSFSW

pinpointed in the TMAZ. Hardness variations between the FSW and the SSFSW joints are attributed to the heat cycle caused by the shoulder. In other words, the stationary shoulder can induce lower heat input to the joint. Thus, thermal softening can be alleviated.

In this simulation, the welding tool remained in contact for 0.5 s following the end of the plunging. The purpose is to ensure a uniform temperature distribution between the advanced and the retreated sides. Figure 7 shows temperature distribution of the cross section following a 0.5 s dwelling process. The maximum temperatures of the FSW and the SSFSW can reach peak values of 570 °C and 550 °C, respectively. The overall temperature of FSW workpieces is generally higher than that of SSFSW. In addition, the temperature gradient between the upper and the lower surfaces is relatively larger. It should be also mentioned that high-temperature “V”-shaped gradient appears in the cross section. This phenomenon illustrates an existence of the high heat flux at the interface between the stirring tool and the workpiece (Ref 20).

Following the dwelling process, the tool moves along the welding direction and the temperature slightly decreases with an increase in the moving distance. Figure 8 shows temperature distributions during the welding process. An interesting phenomenon is observed. The highest temperature does not appear on the edge of the shoulder during the FSW process. This is most likely due to additional heat dissipation of the material located at the shoulder edge. Compared to the FSW, the burrs formed under the combined action of heat and

machinery are eliminated due to the flattening of the stationary shoulder, which is consistent with the actual welding observations.

In both FSW and SSFSW, the heat input directly affects the joint performance. Thus, it is necessary to adequately investigate the welding heat cycles in various areas of the FSW and the SSFSW joints. In Fig. 9, thermal cycles at various locations in welded joints are presented. Coordinate X indicates the distance from the weld line, while coordinate Z indicates the distance from the top surface of the workpiece. According to the microstructure distribution characteristics, points A1 and A2 are located in NZ, while points B1 and B2 are located near TMAZ. The range of HAZ is defined from $X = 4$ mm to $X = 10$ mm. According to Fig. 9, NZ has the highest peak temperature with the values of 530° (FSW) and 490° (SSFSW). The peak temperature and the high-temperature residence time constantly decreases with an increase in the weld line distance. Regarding the welding peak temperature, SSFSW demonstrates lower values compared to the FSW for the welding thermal cycle in the same position.

Figure 10 illustrates the material flow behavior on horizontal planes (near the top of the workpiece) for FSW and SSFSW simulations. In FSW, the range covered by the velocity field is approximately same size as the shoulder at the top surface of the workpiece ($Z = 4$ mm). The speed gradually decreases from the edge to the center of the stirring shoulder. The material flow is strongest at the top surface under direct action from the stirring shoulder. Both flow velocity and the flow region decrease with an increase in depth. This effect can be attributed

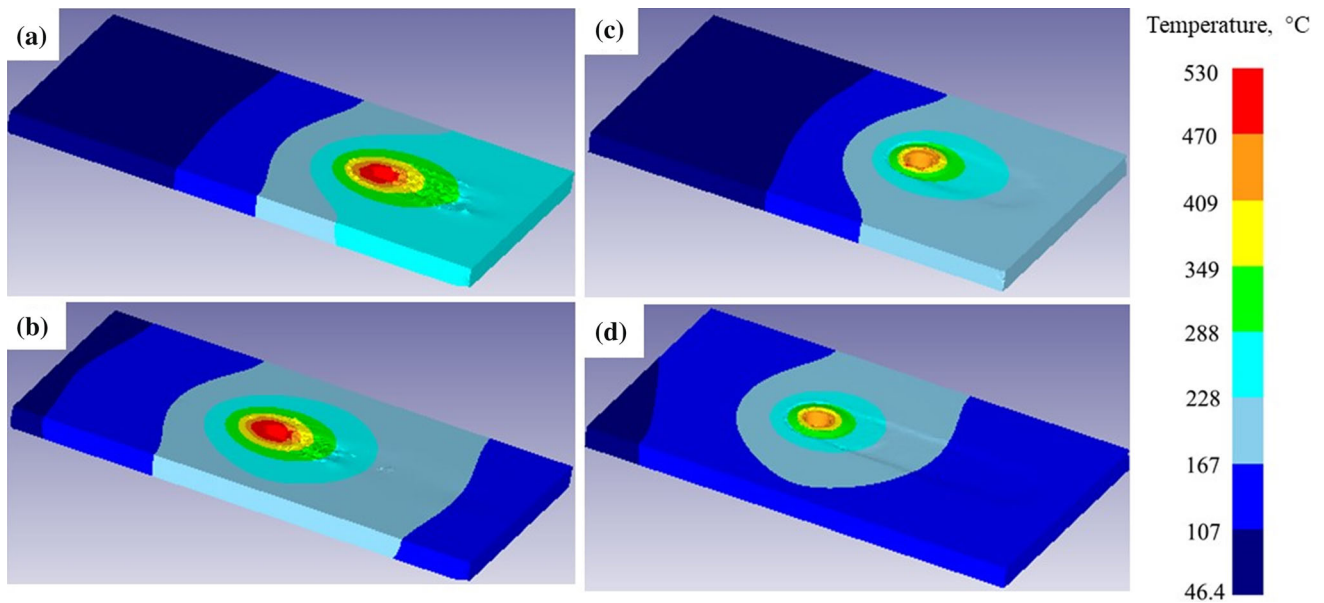


Fig. 8. Temperature distributions in the workpiece: (a) FSW, mid-length, (b) FSW, end of weld, (c) SSFSW, mid-length, and (d) SSFSW, end of weld

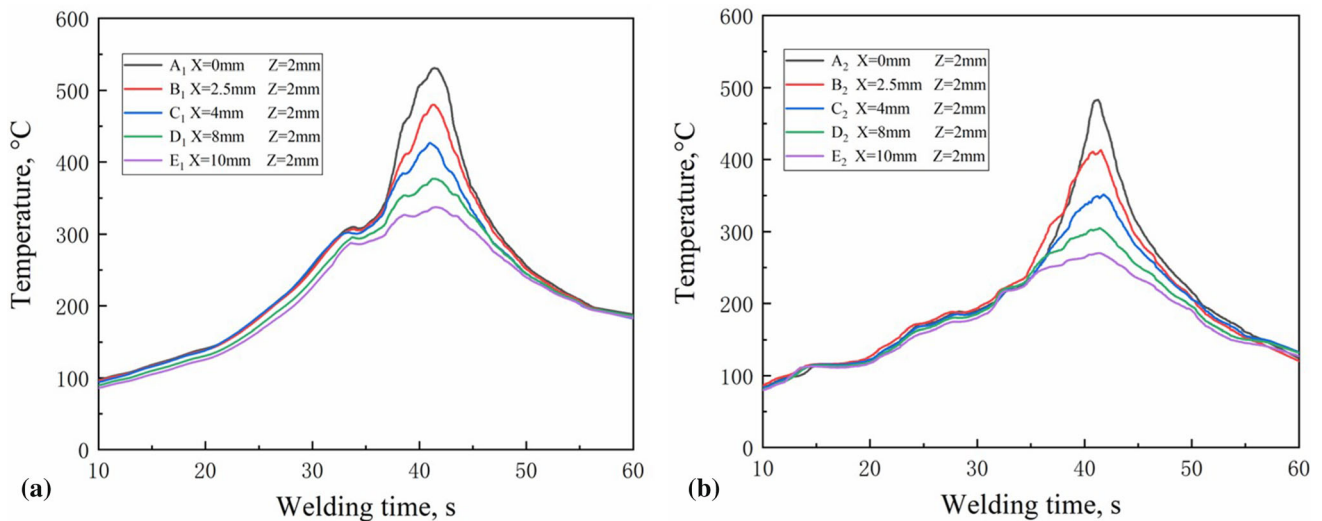


Fig. 9. Thermal cycles at different locations in welded joints: (a) FSW, (b) SSFSW

to the reduced influence of the stirring. For SSFSW, the material flow of the workpiece is different from that of FSW, particularly at the top surface. As demonstrated in Fig. 10(b), only the material near the stirring pin rotates and the material near the shoulder moves along the welding direction. It should be mentioned that the material flow in Fig. 10(d) ($Z = 3 \text{ mm}$) is dominated by rotation, which demonstrates that the stationary shoulder only acts at the top surface of the workpiece.

The velocity field distribution at vertical planes is depicted in Fig. 11. The arrows indicate the direction of the material flow. The material that is located in front of the stirring pin does not flow in the welding direction under the pin extrusion. In contrast, the material is transported backward under the action of the rotational movement (Ref 21, 22). Meanwhile, the material behind the stirring pin is backfilled toward the welding direction (Fig. 11a and c). The material flow in the traverse section plane is shown in Fig. 11(b) and (d). The material near

the bottom of the workpiece flows toward the top surface under the action of the stirring pin. However, material flow near the top surface of the workpiece behaves differently due to the various processing forms of the shoulder. The arrows show a more detailed material flow comparison in the top surface. During the FSW process, the material flow is driven by the high-speed rotating shoulder from the AS to RS and eventually backward to the weld line. In contrast, the stationary shoulder only plays the material extrusion role (Fig. 11d). By combining the discussion of the temperature field and the microstructure, it can be concluded that the formation of the joint microstructure is the result of the combined effects of the welding heat input and mechanical stirring.

Figure 12 shows the effective strain in the cross section. The strain profiles are also “V” shaped, which is analogous to the previously mentioned temperature distributions (Fig. 8). It is evident that the effective strain area in the FSW joints is larger

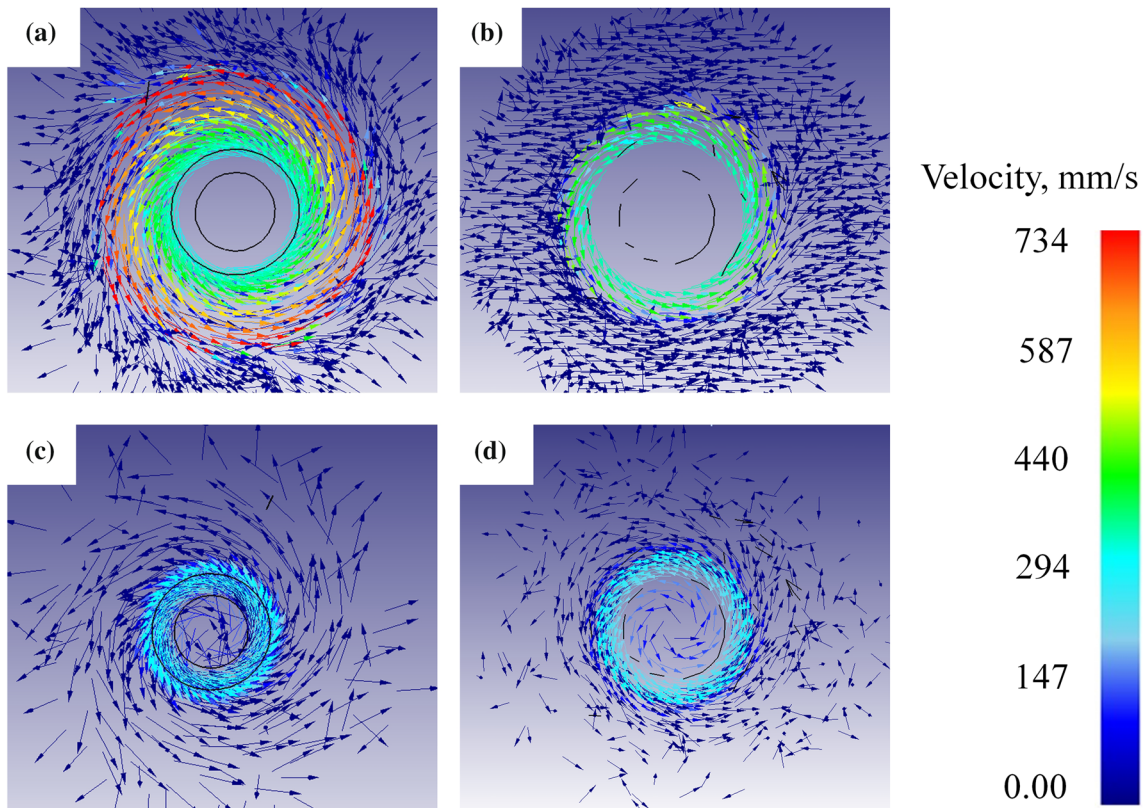


Fig. 10. Velocity field distribution at different horizontal planes: (a) FSW, plane $Z = 4$ mm; (b) SSFSW, plane $Z = 4$ mm; (c) FSW, plane $Z = 3$ mm; (d) SSFSW, plane $Z = 3$ mm

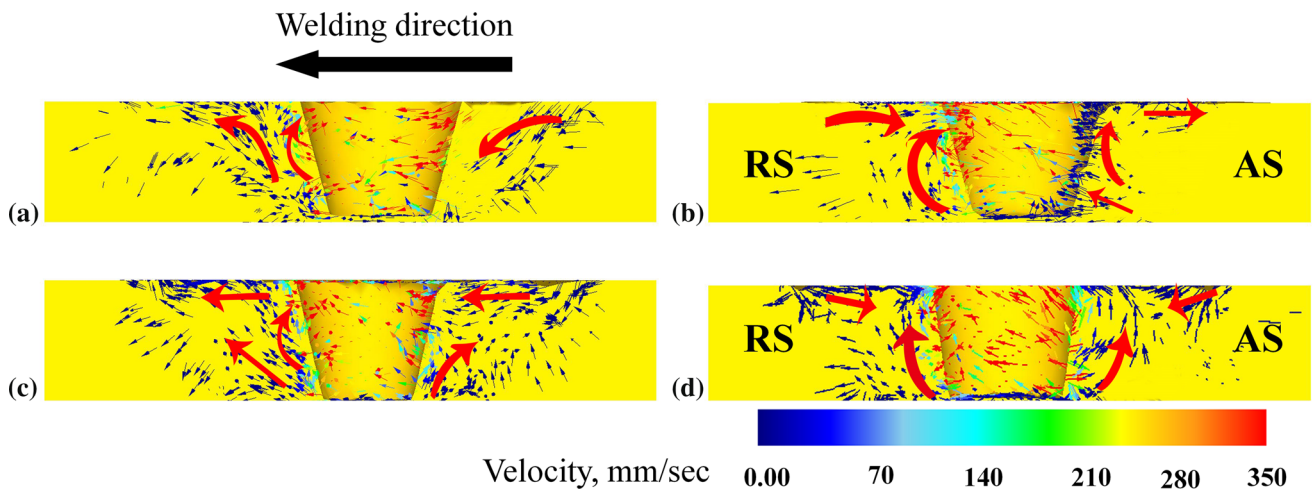


Fig. 11. Velocity field distribution at vertical planes: (a-b) FSW; (c-d) SSFSW; (a, c) vertical plane of the longitudinal section; (b, d) vertical plane of the traverse direction)

due to the stirring action of the shoulder which involves wider area. However, the maximum value shows negligible increase in the stirring pin action area.

Figure 13 shows a comparison of the simulated strain rates at different tracked positions in FSW and SSFSW; point locations on the transverse cross section are presented in Fig. 13(a). The P1 and P2 are located on the weld line, while

P3, P4, P5, and P6 are located on the AS line 2, 4, 8, and 10 mm away from the weld line, respectively. P1 tracked position is made at 3.7 mm above the bottom surface of the workpiece, while other points others are 2 mm above that. In Fig. 13(b) and (c), comparison between the strain rates in FSW and SSFSW is presented, respectively. During the SSFSW process, a significantly higher strain rate can be observed

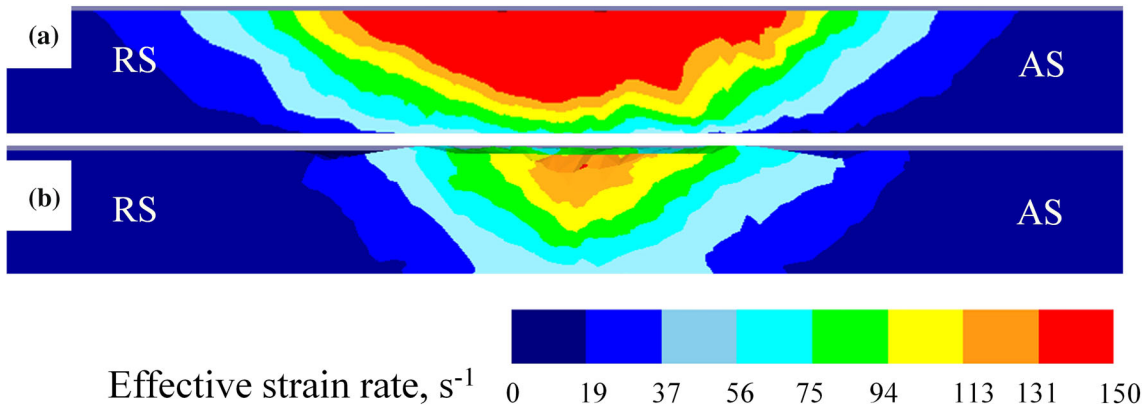


Fig. 12. Effective strain in the cross section: (a) FSW, (b) SSFSW

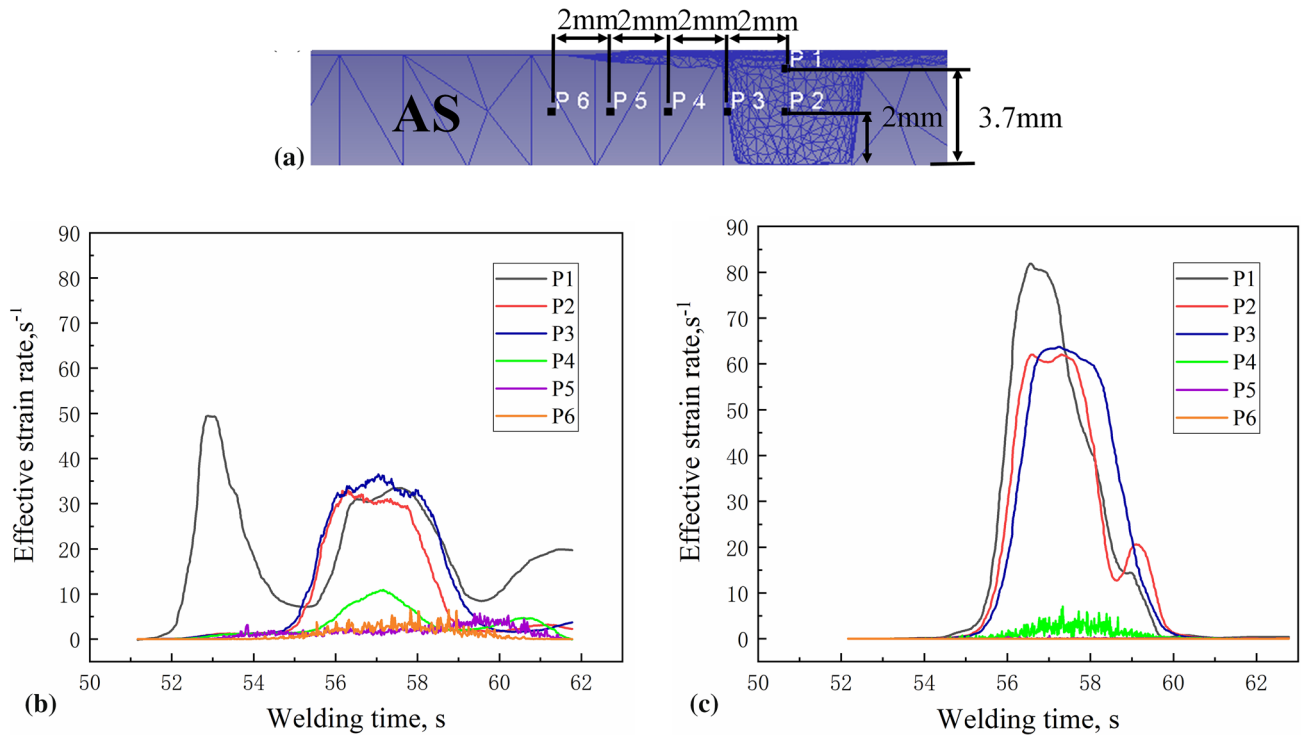


Fig. 13. Strain rates at different tracked positions in the cross section: (a) the point locations on transverse cross section, (b) strain rates during the FSW process, (c) strain rates during the SSFSW process

compared to the FSW. This is mainly because Al-Cu is a heat-softening aluminum alloy, and the flow stress is decreased at higher temperatures (Ref 23, 24). In other words, under the action of the stirring shoulder, the workpiece temperature is increased during the FSW process and the fluidity is improved when compared to the SSFSW. The sliding between the material and the tool is more significant. Therefore, even if the effective strain is relatively large, the local material deformation rate is low. This is the reason for the increased SSFSW strain rate when compared against the FSW (Ref 25). It is interesting to note that the material in P1 experiences two strain rate increasing-decreasing processes. Initial strain rate increase can be attributed to the material entering the shoulder action area. As the welding tool moves, P1 is gradually moved away from the shoulder edge, which decreases the stirring effect. As a

result, the strain rate begins to decrease. Eventually, the strain rate is increased once again by the stirring pin effect.

5. Discussion

5.1 Microstructure Formation Characteristic

In this paper, two main microstructure cross section differences in the FSW and the SSFSW are demonstrated. The first difference is the cross section microstructure homogeneity in both FSW and the SSFSW, while the other difference is the NZ /TMAZ interface sharpness in both processes.

Previously conducted studies (Ref 26, 27) have demonstrated that continuous dynamic recrystallization (CDRX) and

discontinuous dynamic recrystallization (DDRX) are the dominant microstructural evolution mechanisms in the NZ and the TMAZ. Regarding microstructure homogeneity, numerical simulation results indicate that the SSFSW has a lower heat input and a narrower effective strain zone. The occurrence of the CDRX and DDRX requires higher temperatures and sufficiently large strains (Ref 28). Therefore, equiaxed crystals with CDRX characteristics only appear in the stirring pin action area (P1, P2, and P3 in Fig. 13c). However, during FSW, the upper surface has a larger strain and higher relative temperature due to the rotating shoulder. This leads to an inhomogeneous microstructure in the thickness direction. Meanwhile, by combining Fig. 9 and 13 with the range of the TMAZ, it can be observed that TMAZ microstructure characteristic is still not formed at 4 mm from the weld line (C1). This suggests that TMAZ formation is mainly affected by the strain rate. This effect is clear even though the C1 position (Fig. 9a) in FSW experiences a higher welding thermal cycle, which is almost equal to the temperature of B2 in SSFSW.

Regarding the interface sharpness, the NZ/TMAZ interface characteristics mainly depend on the material flow behavior. According to Fig. 5, grains of TMAZ are relatively slim and elongated, while the range of TMAZ is homogeneous in the thickness direction during the SSFSW. On the contrary, the cross section microstructure of FSW illustrates that the TMAZ area gradually decreases from the top surface to the bottom surface, while the NZ/TMAZ interface transition can be considered relatively smooth. The flow behavior in Fig. 11(b) and (d) can explain this phenomenon. The material near the bottom of the pin is thrust upward and the grains are elongated under the action of thermal and mechanical stress, which eventually forms the TMAZ microstructure. During the SSFSW process, the material is mainly subjected to shear forces and it flows along the rotating direction, which leads to the homogeneous microstructure profile. During FSW, in addition to the shear force generated by the pin, the material is also affected by the upsetting force generated by the stirring shoulder. The material flow direction in the near-shoulder position is repositioned toward the weld line, while NZ/TMAZ interface transition is relatively smooth. In addition, guided by the above-mentioned flow mechanism, the NZ/TMAZ interface at the AS is sharper than the interface at the RS. In summary, the stationary shoulder can be utilized to obtain microstructural homogeneity.

5.2 Weld Joint Softening Characteristics

The FSW joints are formed under the combined action of both heat and machinery. Therefore, the strengthening mechanism of welded joints is relatively complicated. It includes grain refinement strengthening, dislocations strengthening, and precipitation hardening. The strengthening mechanism can be summarized as:

$$\sigma_y = \sigma_0 + \Delta\sigma_{H-P} + \Delta\sigma_P + \Delta\sigma_{dis} \quad (\text{Eq } 3)$$

where σ_y is the overall increment, σ_0 is the intrinsic yield strength, $\Delta\sigma_{H-P}$ is grain refinement increment, $\Delta\sigma_P$ is the precipitation hardening, and $\Delta\sigma_{dis}$ is dislocations strengthening (Ref 29). For the Al-Cu alloy, the precipitation hardening is the main strengthening mechanism (Ref 30, 31). According to the microhardness distribution in Fig. 6, the thermal softening of

the SSFSW joint is lower and the microhardness gradient is significantly larger than that of FSW. Despite the relatively small equiaxed crystals and many dislocations within the NZ and TMAZ, softening is still the most serious issue. This is due to almost complete dissolution and precipitation of the second phase. In HAZ, the second phase is coarsened during the welding thermal cycle, which results in deterioration of the strengthening effect. By observing both Fig. 6 and the thermal cycle of E2 in Fig. 9b), it can be concluded that for temperatures lower than 250 °C and high-temperature residence time less than 10 s, the Al-Cu alloy is not softened.

6. Conclusions

In this paper, material flow and temperature distribution during the FSW and SSFSW of AA2219-T6 aluminum alloy were investigated by both numerical simulations and experimental investigations. The following conclusions are made:

1. Numerical simulations are developed to investigate the material flow and temperature profile during FSW and SSFSW. The results obtained via numerical simulations are in good agreement with the experimental results.
2. The joints welded by both FSW and SSFSW can be divided into the following zones: base material, heat-affected zone, thermal-mechanically affected zone, and the nugget zone. The SSFSW joint has a narrower thermal softening zone. Contrary to the results from previous studies, the microhardness test results indicate that the minimum joint hardness of these two welding methods is similar for Al-Cu alloys.
3. The highest temperature peak is obtained during the dwelling stage, where the maximum temperature value gradually decreased and eventually stabilized. The overall temperature of the workpiece welded by SSFSW was lower than that of FSW. The material flow is strongest in the top surface of the workpiece, and it gradually decreases along the workpiece thickness direction. Meanwhile, the material flow behavior revealed the reason that the microstructure of SSFSW is homogenous as previously reported. This is because the material near the stirring tool is only dominated by shear forces during the SSFSW process. In addition, a lower effective strain with higher strain rate is also obtained in the SSFSW process.

Acknowledgments

Financial support for this work was supported by the Key areas Research and Development Program of Guangdong Province (2019B090921003), the National Natural Science Foundation of China (51905112), by the Science and Technology Plan Project of Guangzhou City (201807010063), and by the International Science and Technology Cooperation Project of Guangzhou Economic and Technological Development Zone (2019GH15). The authors are grateful to Wuxi Turbine Blade Co., Ltd for providing software 'DEFORM' support and engineer Ji Liu supports.

References

1. M. Xu, B. Liu, Y. Zhao et al., Direct Joining of Thermoplastic ABS to Aluminum Alloy 6061-T6 Using Friction Lap Welding, *Sci. Technol. Weld. Join.*, 2020 <https://doi.org/10.1080/13621718.2020.1719304>
2. Y. Chen, H. Liu and J. Feng, Friction Stir Welding Characteristics of Different Heat-Treated-State 2219 Aluminum Alloy Plates, *Mater. Sci. Eng. A.*, 2006, **420**(1–2), p 21–25
3. V. Pandian and S. Kannan, Numerical Prediction and Experimental Investigation of Aerospace-Grade Dissimilar Aluminum Alloy by Friction Stir Welding, *J. Manuf. Process.*, 2020, **54**, p 99–108
4. P.L. Threadgill, A.J. Leonard, H.R. Shercliff et al., Friction Stir Welding of Aluminum Alloys, *Int. Mater. Rev.*, 2009, **54**(2), p 49–93
5. J. You, Y. Zhao, C. Dong et al., Microstructure Characteristics and Mechanical Properties of Stationary Shoulder Friction Stir Welded 2219-T6 Aluminum Alloy at High Rotation Speeds, *Int. J. Adv. Manuf. Technol.*, 2019 <https://doi.org/10.1007/s00170-019-04594-1>
6. J.Q. Li and H.J. Liu, Effects of Tool Rotation Speed on Microstructures and Mechanical Properties of AA2219-T6 Welded by the External Non-rotational Shoulder Assisted Friction Stir Welding, *Mater. Des.*, 2013, **43**, p 299–306
7. T. Sun, M.J. Roy, D. Strong et al., Comparison of Residual Stress Distributions in Conventional and Stationary Shoulder High-Strength Aluminum Alloy Friction Stir Welds, *J. Mater. Process. Technol.*, 2017, **242**, p 92–100
8. H. Wu, Y.C. Chen, D. Strong et al., Stationary Shoulder FSW for Joining High Strength Aluminum Alloys, *J. Mater. Process. Technol.*, 2015, **221**, p 187–196
9. S. Sinhmar and D.K. Dwivedi, Mechanical Behavior of FSW Joint Welded by a Novel Designed Stationary Shoulder Tool, *J. Mater. Process. Technol.*, 2020, **277**, p 116482
10. H. Su, C.S. Wu, M. Bachmann et al., Numerical Modeling for the Effect of Pin Profiles on Thermal and Material Flow Characteristics in Friction Stir Welding, *Mater. Des.*, 2015, **77**, p 114–125
11. L. Fratini, G. Buffa, D. Palmeri et al., Material Flow in FSW of AA7075-T6 Butt Joints: Numerical Simulations and Experimental Verifications, *Sci. Technol. Weld. Join.*, 2006, **11**(4), p 412–421
12. B. Vicharapu, H. Liu, H. Fujii et al., Probing Residual Stresses in Stationary Shoulder Friction Stir Welding Process, *Int. J. Adv. Manuf. Technol.*, 2020, **106**(5), p 1573–1586
13. Q. Wen, W.Y. Li, W.B. Wang et al., Experimental and Numerical Investigations of Bonding Interface Behavior in Stationary Shoulder Friction Stir Lap Welding, *J. Mater. Sci. Technol.*, 2019, **35**(1), p 192–200
14. Y. Zhao, H. Liu, T. Yang et al., Study of Temperature and Material Flow During Friction Spot Welding of 7B04-T74 Aluminum Alloy, *Int. J. Adv. Manuf. Technol.*, 2016, **83**(9–12), p 1467–1475
15. H. Pashazadeh, A. Masoumi and J. Teimournezhad, Numerical Modelling for the Hardness Evaluation of Friction Stir Welded Copper Metals, *Mater. Des.*, 2013, **49**, p 913–921
16. L. Fratini, G. Buffa and R. Shivpuri, Mechanical and Metallurgical Effects of in Process Cooling During Friction Stir Welding of AA7075-T6 Butt Joints, *Acta Mater.*, 2010, **58**(6), p 2056–2067
17. H. He, Y. Yi, J. Cui et al., Hot Deformation Characteristics and Processing Parameter Optimization of 2219 Al Alloy Using Constitutive Equation and Processing Map, *Vacuum*, 2019, **160**, p 293–302
18. H. Schmidt and J. Hattel, A Local Model for the Thermomechanical Conditions in Friction Stir Welding, *Model. Simul. Mater. Sci. Eng.*, 2004, **13**(1), p 77
19. Q. Wen, W.Y. Li, Y.J. Gao et al., Numerical Simulation and Experimental Investigation of Band Patterns in Bobbin Tool Friction Stir Welding of Aluminum Alloy, *Int. J. Adv. Manuf. Technol.*, 2019, **100**(9–12), p 2679–2687
20. R. Hamilton, D. MacKenzie and H. Li, Multi-Physics Simulation of Friction Stir Welding Process, *Eng. Comput.*, 2010 <https://doi.org/10.1108/02644401011082980>
21. R. Fonda, A. Reynolds, C.R. Feng et al., Material Flow in Friction Stir Welds, *Metall. Mater. Trans. A.*, 2013, **44**(1), p 337–344
22. G.R. Cui, Z.Y. Ma and S.X. Li, Periodical Plastic Flow Pattern in Friction Stir Processed Al-Mg Alloy, *Scr. Mater.*, 2008, **58**(12), p 1082–1085
23. L. Liu, Y. Wu, H. Gong et al., A Physically Based Constitutive Model and Continuous Dynamic Recrystallization Behavior Analysis of 2219 Aluminum Alloy During Hot Deformation Process, *Materials.*, 2018, **11**(8), p 1443
24. G. Chen, Z. Feng, Y. Zhu et al., An Alternative Frictional Boundary Condition for Computational Fluid Dynamics Simulation of Friction Stir Welding, *J. Mater. Eng. Perform.*, 2016, **25**(9), p 4016–4023
25. R. Kumar, V. Pancholi and R.P. Bharti, Material Flow Visualization and Determination of Strain Rate During Friction Stir Welding, *J. Mater. Process. Technol.*, 2018, **255**, p 470–476
26. H. Liu and H. Fujii, Microstructural and Mechanical Properties of a Beta-Type Titanium Alloy Joint Fabricated by Friction Stir Welding, *Mater. Sci. Eng. A.*, 2018, **711**, p 140–148
27. P.B. Prangnell and C.P. Heason, Grain Structure Formation During Friction Stir Welding Observed by the ‘Stop Action Technique,’ *Acta Mater.*, 2005, **53**(11), p 3179–3192
28. N. Dudova, A. Belyakov, T. Sakai et al., Dynamic Recrystallization Mechanisms Operating in a Ni-20% Cr Alloy Under Hot-to-Warm Working, *Acta Mater.*, 2010, **58**(10), p 3624–3632
29. O.R. Myhr, Ø. Grong and S.J. Andersen, Modelling of the Age Hardening Behaviour of Al-Mg-Si Alloys, *Acta Mater.*, 2001, **49**(1), p 65–75
30. C. Genevois, A. Deschamps, A. Denquin et al., Quantitative Investigation of Precipitation and Mechanical Behaviour for AA2024 Friction Stir Welds, *Acta Mater.*, 2005, **53**(8), p 2447–2458
31. J.Q. Li and H.J. Liu, Characteristics of the Reverse Dual-Rotation Friction Stir Welding Conducted on 2219-T6 Aluminum Alloy, *Mater. Des.*, 2013, **45**, p 148–154

Publisher's Note Springer Nature remains neutral with regard to jurisdictional claims in published maps and institutional affiliations.